

Gravitational wave generation by interaction of high power lasers with matter using shock waves

Hedvika Kadlecová^{1a}, Ondřej Klimo^{1,2}, Stefan Weber¹, and Georg Korn¹

¹ Institute of Physics of the ASCR, ELI–Beamlines project, Na Slovance 2, 18221, Prague, Czech Republic

² FNSPE, Czech Technical University in Prague, 11519 Prague, Czech Republic

Received: date / Revised version: date

Abstract Gravitational wave generation by a strong shock wave in the interaction of high power laser with matter is analyzed in linear approximation of gravitational theory. The analytical formulas and estimates are derived for the metric perturbations and the radiated power of the generated gravitational waves. Furthermore the characteristics of polarization and the behavior of test particles are investigated in the presence of gravitational wave which will be important for the detection.

Key words. gravitational waves – laser – plasma interaction – generation of gravitational waves

PACS. 52.38.-r – 04.30.Db – 52.27.Ey – 52.38.Kd

1 Introduction

The direct detection of gravitational waves remained one of the biggest challenges of experimental physics since the original paper by Einstein in 1918 [1] till February 2016 when interferometer measurements on LIGO and VIRGO confirmed the prediction [2]. Their existence was indirectly shown thanks to the analytical work on radio pulses by Taylor and Hulse in 1974 who first recognized the pulsar PSR 1913+16 in a binary system [3]. The discovered pulsar was a unique binary pulsar which served as a perfect astrophysical laboratory for observations of very strong relativistic effects [4].

The motivation for today's expensive experiments is the understanding of the universe and strong astrophysical sources because the gravitational waves carry the properties of the original source. By their detection we can obtain more information about the stars and the whole universe. The information is hidden in the direction, amplitude, frequency and polarization of gravitational waves. The recent detection will definitely open a new era of experimental physics and astronomy.

The greatest obstacle in the detection of gravitational waves is that their intensity is very weak compared to electromagnetic waves. The gravitational force is the weakest one in the universe but affects the mass effectively on large distances and dominates the physics processes in the universe.

Recent interests in astrophysical sources of high frequency gravitational waves (HFGW) with frequencies $\nu > 100$ kHz, GHz and higher lead to consider and revise the so called GW Hertz experiment which consists of generation and detection of the GW signal in terrestrial laboratories.

The Hertz experiments in the high frequency domain were investigated by Chapline [5] and the well-known experimental group of Rudenko [6]. Namely, Rudenko suggested an experiment associated with high power electromagnetic waves and acoustic impulsive or shock waves travelling and interacting with a non-linear opto-acoustic media. Since lasers are the most powerful sources of electromagnetic radiation on Earth we can assume models where gravitational waves are produced by interaction of laser with mediums in different setups as was suggested in [7,8].

The gravitational waves are produced in space, for example, by non-symmetrical collaps of a star or by two black holes rotating tightly around each other. Such radiation has a quadrupole character. The quadrupole moment is the lowest multipole, whose change generates gravitational waves. In other words, the time derivatives of the quadrupole moment up to third order should be non-zero, see Eqs. (8) and (11).

When an intense laser pulse interacts with foil target, the target starts to be ionized at the surface and free electrons are heated to a very high temperatures. Their thermal expansion from the target surface is accompanied by acceleration of mass inward due to momentum conservation and a shock wave eventually builds up. Such process is non-symmetrical as the mass expanding outward is of low density whereas the mass contained in the shock is compressed to high density. Also the quadrupole moment of plasma changes in time thanks to the change of mass contained in the shock wave and possibly increasing its velocity as the interaction proceeds. Therefore gravitational waves can be generated in this process and with the advent of high energy lasers, the process of generating such waves starts to be an interesting scientific problem.

^a e-mail: hedvika.kadlecova@eli-beams.eu

The first attempts to detect gravitational waves from space were performed by Weber in the low frequency domain [9]. The Weber experiment constructed in 1960s consisted of a tube resonant detector. The detectors sensitivity was about $h \approx 10^{-16}$ which is still smaller than the amplitude of gravitational waves coming from space on Earth which is about 10^{-18} . The measurements made by Weber were not reproduced and it is assumed that some systematic mistake of the experiment was measured instead of gravitational waves. The work was followed by many groups. Today, the Weber type of detectors have sensitivities of $< 10^{-19}$ for example at Louisiana university where they use two-mode superconducting transducer and amplifier (SQUID) in the frequency range < 100 Hz. Other examples are the projects as MiniGrail [10] and Auriga in Padova (Italy) [11, 12].

The gravitational waves (GW) generated from astrophysical sources are searched for by large gravitational interferometer detectors such as the American LIGO [13, 14] and Italian–French VIRGO [15], for a review see [16]. These detectors look for waves in the low frequency spectral band between 10 Hz and 20 kHz. The sensitivity of the LIGO type interferometers is about $h = 10^{-23}$ which would allow to detect weak gravitational waves coming from supernova in our galaxy or Magellanic Cloud. The experiments under construction are space-based interferometers, such as LISA [17] and DECIGO [18]. The vacuum environment would enable the interferometers to work without on Earth based noise. LISA would operate with $h > 10^{-22}$ and in low frequency mode in mHz with launch on L3 ESA program in 2032. Other experiments in this area are GEO600 [19] and CEGO (China) [20].

Gravitational waves can be detected by many other techniques. They can be measured by change of lengths by extremely sensitive interferometers, piezoelectric crystals [21], superconductors, resonance chambers and by conversion of gravitational waves to electromagnetic waves by the Gertsenshtein effect [22, 23] or by sensors [24].

The main purpose of this paper is to correctly analyze generational model, shock wave model, of high frequency gravitational waves (HFGW) in the interaction of high power laser pulse with matter. The model was suggested in [7, 8] together with ablation model [25] and the piston model [26]. The piston and light-sail models of ion acceleration have been analyzed in the context of gravitational waves in more details [27]. We investigate the polarization of the generated gravitational waves and the behavior of test particles in the gravitational field of the wave.

We suggest the generator type of gravitational wave experiment. The resulting perturbations of the waves are of magnitude about 10^{-40} which is out of range of today's known detectors. The technology of detectors as interferometers or resonant chambers for low frequency gravitational waves is useless for the high frequency range and a different technology is required. The detection problem of the generated GW is not addressed in this paper. The feasibility of detection of waves in high frequency regime is discussed for example in [28] for X-ray lasers, their detection in microwave band was discussed in [23], detection by optically-levitated sensors with slightly higher frequency range than advanced LIGO was considered in [22].

In 2011, a new detection scheme was proposed, called Li–Baker detector of HFGW [29], which might have sensitivities 10^{-32} at 10 GHz while the minimal detectable perturbation reaches 10^{-37} . The detector is based on coupling between electromagnetic waves and GW in generalized inverse Gertsenshtein effect [30]. The scheme has also many opponents, [31], and is considered as non–realistic. Another technology should be developed to detect HFGW in the future.

The remainder of the paper is organized as follows. In Sect. 2 we review the basic theory of linearized gravity which we will use throughout the paper. We present the notation, the metric, the limitations of the theory, the analytical expression for perturbations and the luminosity, the polarization of the gravitational radiation and the test particles behavior in the slow motion and distant field approximation of the linearized gravitational theory.

In Sect. 3, we review the assumed shock wave model of the experiment for the gravitational waves generation under laboratory conditions. We derive the analytical formulas for the space perturbations and the luminosity of the gravitational radiation and give estimates for an experiment with megajoule class lasers.

In Sect. 4 we derive and analyze the polarization properties of the gravitational radiation and the different radiative properties with dependence on the orientation of the wave vector in the assumed shock wave model.

Section 5 concentrates on derivation and analysis of the behavior of the test particles in the field of passing gravitational waves in the presented shock wave model.

The main results are summarized in the concluding Sect. 6.

2 Linearized gravitational theory for gravitational waves studies

In this Sect., we review the basics of linearized theory of gravitation [32, 33, 4] needed for the subsequent analysis. We will use it to set up the notation which will be analyzed throughout the paper according to [32].

2.1 The basics of the theory

The linearized theory of gravitation assumes the existence of a coordinate system in spacetime where the metric is close to the Minkowski flat metric $\eta_{\mu\nu}$ as

$$g_{\mu\nu} = \eta_{\mu\nu} + h_{\mu\nu}, \quad |h_{\mu\nu}| \ll 1, \quad (1)$$

where the perturbation of the metric is denoted as $h_{\mu\nu}$ and the Einstein equations read

$$\square \bar{h}_{\mu\nu} = -\frac{16\pi G}{c^4} T_{\mu\nu}, \quad \partial^\nu \bar{h}_{\mu\nu} = 0, \quad \bar{h}_{\mu\nu} = h_{\mu\nu} - \frac{1}{2} \eta_{\mu\nu} h, \quad (2)$$

where $\square = \frac{1}{c^2} \frac{\partial^2}{\partial t^2} - \Delta$ is the d'Alembert operator, $T_{\mu\nu}$ is the stress–energy tensor, G is gravitational constant and c is the velocity of light. We have used the Lorentz gauge which reduces ten independent components of the 4×4 matrix $h_{\mu\nu}$ to six independent components. The Eqs. (2) satisfy the conservation of energy–momentum for consistency, $\partial^\nu T_{\mu\nu} = 0$.

2.2 The plane wave solution, TT gauge and polarization

We want to investigate the propagation of gravitational waves and their interaction with test particles (and therefore with their detector) therefore we are interested in the solutions of (2) outside of the sources $\bar{\square}\bar{h}_{\mu\nu} = 0$, $T_{\mu\nu} = 0$. We consider the simplest solution for the wave equation (2) which is the plane wave solution,

$$\bar{h}_{\mu\nu} = \text{Re} \left[A_{\mu\nu} \exp(ik_\alpha x^\alpha) \right], \quad (3)$$

where the $A_{\mu\nu}$ amplitude and k_α wave vector satisfy $k_\alpha k^\alpha = 0$. The k_α is a null vector and $A_{\mu\nu} k^\alpha = 0$ so that $A_{\mu\nu}$ is orthogonal to k_α . The solution describes a wave with frequency $\omega/c \equiv k^0 = (k_x^2 + k_y^2 + k_z^2)^{1/2}$ which propagates with the speed of light in the direction $(1/k^0(k_x, k_y, k_z))$. The spatial components \bar{h}_{ij}^{TT} of perturbation metric $h_{\mu\nu}^{TT}$ in TT gauge¹ are obtained as

$$\bar{h}_{ij}^{TT} = \Lambda_{ij,kl} h_{kl}, \quad (4)$$

where

$$\Lambda_{ij,kl}(\mathbf{n}) = P_{ik}P_{jl} - \frac{1}{2}P_{ij}P_{kl} = \delta_{ik}\delta_{jl} - \frac{1}{2}\delta_{ij}\delta_{kl} - n_j n_l \delta_{ik} - n_i n_k \delta_{jl} + \frac{1}{2}n_k n_l \delta_{ij} + \frac{1}{2}n_i n_j \delta_{kl} + \frac{1}{2}n_i n_j n_k n_l. \quad (5)$$

The projector operator is $P_{jk}(\mathbf{n}) = \delta_{jk} - n_j n_k$ and $n_k = k_k/k$ is the unit vector in the direction of propagation. Note that this projector method is valid only for plane waves, [4].

2.3 The weak field sources with arbitrary velocity

The Eqs. (2) can be solved using Green functions and the leading term reads at the large distances as

$$h_{ij}^{TT}(t, \mathbf{x}) = \frac{4G}{rc^4} \Lambda_{ij,kl}(\mathbf{n}) \int d^4 x' T_{kl} \left(t - \frac{r}{c} + \frac{\mathbf{x}' \cdot \mathbf{n}}{c}, \mathbf{x}' \right). \quad (6)$$

Our convention for four-vector $k^\mu = (\omega/c, \mathbf{k})$ and $x^\mu = (ct, \mathbf{x})$ and then $k_\mu x^\mu = -\omega t + \mathbf{k} \cdot \mathbf{x}$ and $r = |\mathbf{x} - \mathbf{x}'|$.

2.4 The low velocity multipole expansion

In the non-relativistic system, ($v \ll c$) and the reduced wavelength of the radiation generated is much bigger than the size of the system,

$$v \ll c \implies \lambda \gg l_d, \quad (7)$$

where the linear size of the source is denoted as l_d and reduced wavelength $\lambda = \lambda/2\pi$, [32]. If this condition is valid we do not need to know the internal motions of the source and therefore the radiation is dominated by the lowest multipole moments.

The perturbation (6) can be expressed in multipole expansion, see [32, 33, 4]. The lowest moment for gravitational waves is the quadrupole moment, the dipole moment vanishes because of the energy and momentum conservation law. In the following text we will work just in quadrupole approximation, i.e. the lowest term in the moment expansion (6).

¹ We use Latin letters (i, j, \dots) for transverse-space (spatial) indices and the Greek letters (μ, ν) for spacetime indices.

2.5 The mass and quadrupole moment, luminosity

The leading term in the expansion (6) is

$$[h_{ij}^{TT}(t, \mathbf{x})]_{\text{quad}} = \frac{1}{r} \frac{2G}{c^4} \Lambda_{ij,kl}(\mathbf{n}) \ddot{I}^{kl}(t - r/c), \quad (8)$$

where I^{ij} denotes the quadrupole moment defined as

$$I^{ij} = M^{ij} - \frac{1}{3} \delta^{ij} M_{kk} \equiv \int d^3 x \rho(t, \mathbf{x}) (x^i x^j - \frac{1}{3} r^2 \delta^{ij}), \quad \rho = \frac{1}{c^2} T^{00}, \quad (9)$$

and ρ becomes the mass density (in the lowest order in v/c). The mass moment is defined as

$$M^{ij} = \int d^3 x \rho(t, \mathbf{x}) x^i x^j. \quad (10)$$

The total gravitational luminosity (power) of the source in quadrupole approximation is

$$\mathcal{L}_{\text{quad}} = \frac{G}{5c^5} \langle \ddot{I}_{ij} \ddot{I}_{ij} \rangle, \quad (11)$$

where I_{ij} is evaluated in the retarded time $t - r/c$.

In the following text, we consider the entities I_{ij} and h_{ij}^{TT} are evaluated in the retarded time $t - r/c$ and we do not specify that explicitly.

3 The derivation of gravitational wave characteristics for generational shock wave model

This Sect. is devoted to the derivation of fully analytical formulae of the luminosity \mathcal{L}_{GW} and the perturbation of the metric h_{GW} for the shock wave model using the linearized gravity theory from Sect. 2.

3.1 The shock wave model

The shock wave model is described according to the analytical theory of planar laser-driven ablation [25]. The process is a function of the laser intensity, wavelength, the target material, and the degree of inhibition of electron thermal conduction.

In this configuration, the laser is interacting with a planar thick foil of about 1 mm thickness. This thickness corresponds to the distance the shock wave can travel inside the target for the laser and target parameters given in section 3.3.4. The material is accelerated in the ablation zone and in the shock front. These two possibilities are divided into two separate models, the shock wave model and the ablation zone generation model. In the experiment, the two models are present together and the radiation could be measured simultaneously. In this paper, we do not investigate possible interference of the radiation from the two models.

In the shock wave model, the laser launches a shock with the velocity v_s . The material from the foil is accelerated along the axis of motion z and it produces a change of mass – the change of quadrupole mass moment of the source I_{ij} . A typical order of duration is 1 ns therefore the gravitational waves are generated in the GHz domain.

3.2 The limitations of the theory

We assume our models are non-relativistic ($v \ll c$) and the reduced wavelength of the generated radiation must be much bigger than the linear size of the source,

$$\lambda \gg l_d < 1 \text{ mm}, \quad (12)$$

furthermore we assume that the linear size of the source is $l_d < 1$ mm (target thickness).

The reduced generated wavelength is $\lambda = 4.77 \times 10^{-2}$ m. The comparison (7) results into $0.21 \times 10^{-1} \ll 1$, therefore the low velocity condition is still satisfied for our shock wave experiment. In general, according to (12), the condition is satisfied always for any $\lambda \gg 1$ mm. The validity of this condition is much weaker than for a pulsar in space, where the difference is $10^{-15} \ll 1$.

3.3 The Shock wave model calculations

We choose the orthogonal coordinate system x, y, z and we assume the whole process takes place in a box of rectangular shape with parameters a, b, z_L for simplicity. The origin of the coordinate system corresponds to the position where the detector will be positioned.

We assume a rectangular shape of the foil with parameters, a, b, l . The parameter l is the thickness of the foil in the z direction and a, b are the dimensions of the foil in x, y directions. The constant distance between the position of the laser and the detection point is denoted as z_L .

The moving point where the density of the beam changes will be denoted as z_s with the functional dependence

$$z_s(t) = -v_s t + f_1, \quad (13)$$

where the density of the beam changes (i.e. the shock front) and is defined as

$$v_s \simeq \sqrt{\frac{P_s}{\rho_0}}, \quad (14)$$

where P_s is shock wave pressure², ρ_0 is material density and f_1 is the distance from the shock wave front to the detector.

We assume that for $t = 0$, $z_s(0) = f_1$, which is our convenient choice. We also use the decomposition of $f_1 = f + l$, where f is the distance from the detector to the left edge of the foil. Using f_1 , we have defined the time t_{det} (52) when the shock wave reaches the detector and $z(t_{det}) = 0$. We can always perform a shift of the origin by setting $f_1 = 0$, which will simplify some results but we prefer to have the choice in setting the f_1 to any convenient value. We will use general expression for P_s , which will allow us to have control over more parameters than the one used in [8,7] for a fixed wavelength. The relation of P_s and I_L (laser intensity) is the following, [34],

$$P_s = R_t^{1/3} I_L^{2/3}, \quad R_t = \frac{1}{2} \frac{A}{Z} m_p n_c, \quad n_c = \frac{\epsilon_0 m_e (2\pi c)^2}{e^2 \lambda_L^2}, \quad (15)$$

² In the case of subsonic deflagration assumed in this paper, the difference between ablation and shock pressure is neglected, because depending on the energy deposition at the heat front is at most 2 in the stationary ablation model [34].

where R_t denotes the target 'density' (material constant) and n_c is the critical density, ϵ_0 is permittivity of vacuum, m_e is the rest mass of the electron, m_p is the rest mass of the proton, e is the charge of electron, λ_L is the wavelength of the laser, A is the mass number and Z is the atomic number. All of the parameters in n_c are constants except the laser wavelength λ_L which is constant given by the specific experiment. We will keep the constant R_t in general form till substituting some explicit values.

In the following, we will calculate everything with general function $z_s(t)$ and then we will substitute the explicit function (13) at convenient places. General expressions might be useful for other forms of $z_s(t)$. The shock wave density would be

$$\rho(\mathbf{x}) = \begin{cases} 0 & \text{if } f < 0, f > \text{ and } < \frac{f+l-z_s}{4} + z_s, z_L >, \\ \rho_0 & \text{if } < f, z_s >, \\ 4\rho_0 & \text{if } < z_s, \frac{f+l-z_s}{4} + z_s >, \end{cases} \quad (16)$$

such density satisfies the mass conservation in the model contrary to the idealized density (17). To simplify the calculation, the step function for the density profile can be written as

$$\rho(\mathbf{x}) = \begin{cases} \rho_0 & \text{if } z < z_s, \\ 4\rho_0 & \text{if } z_s < z < z_L. \end{cases} \quad (17)$$

The idealized density gives basically same main results, therefore we decided to use the idealized density in the further calculations. To show this, we present the mass moment for the density (16), see discussion below.

3.3.1 The mass moment

The first step in the calculation is the mass moment derivation. We introduce notation on transverse plain to the direction of motion z , the transverse space is covered by two spatial coordinates $x^i = \{x, y\}$, the transverse space is $ds_{\perp}^2 = g_{ij\perp} dx^i dx^j = dx^2 + dy^2$ is flat and we introduce the parameters $\zeta^i = \{a, b\}$ in the transverse space and we use the Latin indices i, j, \dots to label the corresponding tensor components. The mass moment (10) is a 3×3 symmetric matrix in spacelike coordinates, therefore it is necessary to calculate just the components on diagonal M_{ii}, M_{zz} and non-diagonal components M_{ij}, M_{iz} .

The mass moment diagonal components then read

$$M_{ii} = S \zeta_i^2 \rho_0 \left(\frac{4}{3} z_L - z_s \right), \quad M_{zz} = S \rho_0 \left(\frac{4}{3} z_L^3 - z_s^3 \right),$$

and the non-diagonal components M_{ij}, M_{iz} ,

$$M_{ij} = S^2 \rho_0 \left(z_L - \frac{3}{4} z_s \right), \quad M_{iz} = S \zeta_i \rho_0 \left(z_L^2 - \frac{3}{4} z_s^2 \right). \quad (18)$$

These intermediate results will be useful for the polarization because they show that it is sometimes more convenient to use the mass moment for calculations instead of the quadrupole moment.

We also present the mass moment for the density (16),

$$M_{ii} = S \frac{\zeta_i^2}{3} \rho_0 l, \quad M_{zz} = \frac{S}{3} \rho_0 \left(4 \left[\frac{f_1 + 3z_s}{4} \right]^3 - 3z_s^3 - f^3 \right),$$

$$M_{ij} = \frac{S^2}{4} \rho_0 (l - 2z_s), \quad M_{iz} = \frac{S}{64} \zeta_i \rho_0 (-25z_s^2 + 10f_1 z_s + 16f^2 - f_1^2). \quad (19)$$

When we compare the mass moment (19) with the mass moment for simpler density (18), we observe that the terms with time dependent z_s have the same power, apart from M_{ii} component. The additional constants will vanish in derivations, subsequently, the perturbation $h_{\mu\nu}$ and luminosity $\mathcal{L}_{\text{quad}}$ will result in the same functional expressions up to a constant.

3.3.2 The quadrupole moment

The next step is the calculation of the quadrupole moment (9). The second term is none-zero just for the diagonal components which will be more complicated. Then the non-diagonal components I_{ij}, I_{iz} are

$$I_{ij} = M_{ij}, \quad I_{iz} = M_{iz}. \quad (20)$$

The diagonal components $I_{ii} = M_{ii} - \frac{1}{3} TrM$ read

$$I_{ii} = \frac{S\rho_0}{3} \left\{ z_s^3 - (2\zeta_i^2 - \zeta_j^2)z_s + \frac{4}{3} z_L (2\zeta_i^2 - \zeta_j^2 - z_L^2) \right\},$$

$$I_{zz} = \frac{S\rho_0}{3} \left\{ -2z_s^3 + (\zeta_i^2 + \zeta_j^2)z_s + \frac{4}{3} z_L (2z_L^2 - (\zeta_i^2 + \zeta_j^2)) \right\}. \quad (21)$$

We observe that the diagonal components of quadrupole moment show cubic dependence on the function z_s and are missing a quadratic term. The non-diagonal components I_{iz} are missing the linear dependence on z_s .

3.3.3 The analytical form of perturbation and luminosity

Now, we calculate the components of the perturbation tensor according to (8) without projector appearing in (4). In other words, we obtain the components of the perturbation tensor in general form:

$$h_{ij} = -\frac{2G}{3rc^4} S \rho_0 \left\{ (2\zeta_i^2 - \zeta_j^2) \ddot{z}_s - (z_s^3) \ddot{} \right\},$$

$$h_{zz} = \frac{2G}{3rc^4} S \rho_0 \left\{ (a^2 + b^2) \ddot{z}_s - 2(z_s^3) \ddot{} \right\}, \quad (22)$$

and the non-diagonal terms are

$$h_{ij} = -\frac{3G}{2rc^4} S^2 \rho_0 \ddot{z}_s, \quad h_{iz} = -\frac{3G}{2rc^4} S \zeta_i \rho_0 (z_s^2) \ddot{}. \quad (23)$$

After substituting the quadrupole moment components into (11), we get the general expression

$$\mathcal{L}_{\text{quad}} = \frac{G}{45c^5} S^2 \rho_0^2 \left\{ 6[(z_s^3) \ddot{}]^2 - 6\ddot{z}_s (z_s^3) \ddot{} (a^2 + b^2) \right. \quad (24)$$

$$+ (\ddot{z}_s)^2 [(a^2 + b^2)^2 + (2a^2 - b^2)^2 + (2b^2 - a^2)^2 + \frac{81}{8} S^2]$$

$$\left. + \frac{81}{8} (a^2 + b^2) [(z_s^2) \ddot{}]^2 \right\}.$$

The explicit substitution z_s simplifies the expression (24) that just the diagonal components of quadrupole moment contribute to the result, which reads

$$\mathcal{L}_{\text{quad}} = \frac{24G}{5c^5} S^2 \rho_0^2 v_s^6 = \frac{24}{5} \frac{G}{c^5} \frac{R_t}{\rho_0} P_L^2. \quad (25)$$

and further using (14) and (15), we will obtain the final expression for luminosity of gravitational radiation. The luminosity then depends on the power of the laser P_L , the density of the material and the laser wavelength. The numerical factor in front of the fraction for estimation will be presented in the next Subsect. (3.3.4).

The perturbation component h_{zz}^{GW} becomes using (14), (15) and (8),

$$h_{zz} = \frac{8G}{rc^4} \left(\left(\frac{R_t}{\rho_0} \right)^{1/2} E_L - S f_1 R_t^{1/3} I_L^{2/3} \right), \quad (26)$$

where we used the energy of the laser,

$$E_L = S I_L \tau \quad (27)$$

and τ is the laser pulse duration. We have assumed stationary shock wave where the dissipated energy is recovered from the absorbed laser energy, therefore we assume that $t = \tau$, i.e. t is time of shock propagation in the sample. We have obtained additional constant term which reduces the first term in the brackets which is of coordinate nature (vanishes for $f_1 = 0$) and therefore it has no physical meaning.

This is the final formula for the perturbation of the space by gravitational wave in the z direction. When we compare our result with the ones in [8, 7], we observe that the first term in the brackets generalizes the result with the R_t dependency. The value of the perturbation decreases with the distance as $1/r$ and will be zero at infinity. The numerical factors will be evaluated in the next Subsect. (3.3.4) for specific values of the experiment.

3.3.4 The estimations for the $h_{\mu\nu}$ and $\mathcal{L}_{\text{quad}}$ for real experiment

We will evaluate the numerical factors in final results for luminosity (25) and the perturbation h_{zz}^{GW} of the space by the gravitational wave in zz direction, (26), which will be useful for real experiment.

Now, we arrive to the expression for the luminosity as

$$\mathcal{L}_{\text{quad}} [\text{W}] = 1.34 \times 10^{-29} \left[\frac{\text{s}^3}{\text{g cm}^2} \right] \frac{R_t [\text{g/cm}^3]}{\rho_0 [\text{g/cm}^3]} P_L^2 [\text{PW}]. \quad (28)$$

When we compare our result with [7, 8] we observe that our estimation is six orders lower.

Next, we will perform the estimation for the zz component of the perturbation tensor h_{ij} . We will investigate the first time dependent physical part of (26), the second constant term has no physical meaning because we can make it zero by choosing different center of coordinate system with start at $f_1 = 0$ and

therefore we will not discuss its contribution. Similarly to the previous case, we obtain

$$h_{zz} = 6.68 \times 10^{-41} \left[\frac{s^2}{g \text{ cm}} \right] \frac{1}{r[\text{cm}]} \left(\frac{R_t[\text{g/cm}^3]}{\rho_0[\text{g/cm}^3]} \right)^{1/2} E_L[\text{MJ}]. \quad (29)$$

The value of R_t can be estimated either, we have chosen Carbon as a material for the target with $A = 12$, $Z = 6$ and wavelength $\lambda_L = 0.35 \times 10^{-4}$ cm. While using standard constants R_t and n_c in (15), we will obtain

$$R_t = 15.14 \times 10^{-3} [\text{g/cm}^3]. \quad (30)$$

We will evaluate our expressions for experimental values, [8]:

$$\begin{aligned} P_L &= 0.5 \text{ PW}, & \rho_0 &= 30 \text{ mg/cm}^3, & E_L &= 0.5 \text{ MJ}, \\ \tau &= 1 \text{ ns}, \end{aligned} \quad (31)$$

and the detection distance is $r = 10$ m or equivalently $f_1 = f = 10$ m, parameters a, b of the target foil are $a = b = 1$ mm = 10^{-3} m and therefore $I_L = 0.5 \times 10^2$ [PW/cm²]. The parameters of the laser beam chosen roughly correspond to those of the highest energy lasers available (i.e. NIF [35] and LMJ [36]) assuming that all the beams are synchronised and focused to a single focal spot. The reason for this choice is that the metric distortion as given in (26) is directly proportional to laser pulse energy and thus the megajoule class lasers can maximize emission of gravitational waves in this shock wave model. The third-harmonic of the fundamental frequency of these lasers (corresponding to $\lambda = 351$ nm) is assumed to make absorption of the laser light efficient. The outgoing gravitational radiation has frequency $\nu_g = 1$ GHz and wavelength $\lambda_g = 0.3$ m. The final estimations for our expressions of the luminosity and the perturbation are:

$$\mathcal{L}_{GW} \approx 1.69 \times 10^{-30} [\text{W}], \quad h_{zz}^{GW} \approx 2.37 \times 10^{-39}. \quad (32)$$

The orders of the first term of h_{zz} correspond to [7, 8] but the order of \mathcal{L}_{GW} is four orders lower.

4 The polarization of gravitational waves

In this Sect., we are going to investigate the two polarization modes of the gravitational waves which are generated by the models. We derive the amplitudes of the gravitational wave in two independent modes, + and −, and focus on their interpretation which would be useful for real experimental conditions.

We can decompose the gravitational wave into two linearly polarized components or into two circularly polarized components. To decompose the gravitational wave into two independent linearly polarized waves we can rewrite the spatial perturbation tensor in (4) as

$$h_{ij}^{TT}(\mathbf{x}) = h_{+ij} + h_{\times ij}, \quad (33)$$

where we can introduce unit linear tensors of linear polarization as $e_{+ij} = (\mathbf{e}_1)_i(\mathbf{e}_1)_j - (\mathbf{e}_2)_i(\mathbf{e}_2)_j$, $e_{\times ij} = (\mathbf{e}_1)_i(\mathbf{e}_2)_j + (\mathbf{e}_1)_j(\mathbf{e}_2)_i$, where we have denoted \mathbf{e}_1 and \mathbf{e}_2 as unit vectors.

The two independent linearly polarized waves can be written as

$$h_{+ij} = A_+ e^{-i\omega(t-\mathbf{n}\cdot\mathbf{x})} e_{+ij}, \quad h_{\times ij} = A_\times e^{-i\omega(t-\mathbf{n}\cdot\mathbf{x})} e_{\times ij}, \quad (34)$$

where A_+ and A_\times are amplitudes of the two independent polarizations. For example $\mathbf{e}_1 = (1, 0, 0)$ and $\mathbf{e}_2 = (0, 1, 0)$ for the wave vector $\mathbf{n} = (0, 0, 1)$, we will get the result for wave propagation in z coordinate.

We can investigate the gravitational waves in dependence on the direction of the propagation, i.e. on the wave vector. The set up of our models is that the direction of the motion is the z coordinate. Therefore it makes sense to study the wave vectors oriented in the transversal directions x, y . Then we look at the general orientation of the wave vector in spherical coordinates and analyze the space distribution of the gravitational waves from the experiment. These results could help in specifying the exact position for detectors in experiment to measure non-zero values.

4.1 The x, y and z directions of the wave vector

First, we are going to investigate the gravitational perturbations in the direction of the propagation, in the z -coordinate.

4.1.1 The wave propagation in the z -direction

The h_{ij}^{TT} (4) has then the only non-vanishing components as

$$\begin{aligned} h_{xx}^{TT} &= -h_{yy}^{TT} = \text{Re} \left\{ A_+ e^{-i\omega(t+z/c)} \right\}, \\ h_{xy}^{TT} &= h_{yx}^{TT} = \text{Re} \left\{ A_\times e^{-i\omega(t+z/c)} \right\}, \end{aligned} \quad (35)$$

where the wave propagation vector is in the z -direction $\mathbf{n} = (0, 0, -1)$ and A_+, A_\times represent amplitudes of two independent orthogonal modes of polarization. We have used the definition of perturbation tensor (8) expressed conveniently with the mass moment together with the only non-zero components of the projector Λ_{ijkl} (5), $\Lambda_{xx,xx} = \Lambda_{yy,yy} = \frac{1}{2}$, $\Lambda_{yy,xx} = \Lambda_{xx,yy} = -\frac{1}{2}$, $\Lambda_{xy,xy} = \Lambda_{yx,yx} = 1$.

The waves are therefore linearly polarized in the direction of propagation, which follows from the comparison of (35) and the definitions of linear decomposition of gravitational wave (33). We obtain the amplitudes of the polarization modes for the shock wave model in the form, [32],

$$\begin{aligned} A_+ &= \frac{1}{r} \frac{G}{c^4} (\ddot{M}_{xx} - \ddot{M}_{yy}) = \frac{1}{r} \frac{G}{c^4} S \rho_0 \ddot{z}_s (b^2 - a^2), \\ A_\times &= \frac{2}{r} \frac{G}{c^4} \ddot{M}_{xy} = -\frac{3}{2r} \frac{G}{c^4} S^2 \rho_0 \ddot{z}_s. \end{aligned} \quad (36)$$

When we substitute the ansatz for the velocity z_s (13) and its derivatives, we observe that

$$A_+ = A_\times = 0. \quad (37)$$

Therefore the radiation h_{ij}^{TT} is vanishing for the orientation of the wave vector into the direction of motion. The waves do not radiate along the z axis in which the motion occurs.

The result corresponds to the case of quadrupole oscillator example of two mass particles which are connected by a spring oriented in the z direction [33]. This is just a consequence of the geodesic deviation equation (63). The gravitational wave is not just transversal mathematically, i.e. h_{ij}^{TT} , but it has its physical effects. The gravitational radiation is non-zero in the other directions, for example in the direction of the x and y axes, see the next Subjects.

4.1.2 The wave propagation in the x -direction

The h_{ij}^{TT} (4) has the only non-vanishing components for the wave vector in the x -direction $n = (1, 0, 0)$,

$$h_{yy}^{TT} = -h_{zz}^{TT} = \text{Re} \left\{ A_+ e^{-i\omega(t-x/c)} \right\}, \quad h_{zy}^{TT} = h_{yz}^{TT} = \text{Re} \left\{ A_\times e^{-i\omega(t-x/c)} \right\} \quad (38)$$

where we have used again the definition of perturbation tensor (8) together with the only non-zero components of the projector Λ_{ijkl} (5), $\Lambda_{yy,yy} = \Lambda_{zz,zz} = \frac{1}{2}$, $\Lambda_{zz,yy} = \Lambda_{yy,zz} = -\frac{1}{2}$, $\Lambda_{zy,zy} = \Lambda_{yz,yz} = 1$.

The waves are linearly polarized as in the previous case. We obtain the amplitudes of the polarization modes as, [32]:

$$A_+ = \frac{1}{r} \frac{G}{c^4} (\ddot{M}_{yy} - \ddot{M}_{zz}) = -\frac{1}{r} \frac{G}{c^4} S \rho_0 \left[b^2 \ddot{z}_s - (\dot{z}_s^3) \right],$$

$$A_\times = \frac{2}{r} \frac{G}{c^4} \ddot{M}_{yz} = -\frac{3}{2r} \frac{G}{c^4} S \rho_0 b (\dot{z}_s^2). \quad (39)$$

After we use the ansatz for the z_s , we get

$$A_+ = \frac{6}{r} \frac{G}{c^4} S \rho_0 v_s^2 (f_1 - v_s t), \quad A_\times = -\frac{3}{r} \frac{G}{c^4} S \rho_0 b v_s^2. \quad (40)$$

We have obtained non-zero amplitudes for both '+' and 'x' polarization modes. The amplitudes depend on the focus area S , the density of the material ρ_0 and the velocity of the ions v_s . The amplitudes vanish as the radial distance $r \rightarrow \infty$ and it decreases like $1/r$.

Importantly, the amplitude of the '+' polarization is linearly time dependent and the other one \times is not. The time when A_+ vanishes is $t_{det} = f_1/v_s$, i.e. when the shock wave reaches the detector.

The amplitudes of radiation and the radiative characteristics of the radiation are the main results of this paper.

4.1.3 The wave propagation in the y -direction

The perturbation tensor in TT calibration (4) for the wave vector in the y -direction $n = (0, 1, 0)$ reads

$$h_{xx}^{TT} = -h_{zz}^{TT} = \text{Re} \left\{ A_+ e^{-i\omega(t-y/c)} \right\}, \quad h_{zx}^{TT} = h_{xz}^{TT} = \text{Re} \left\{ A_\times e^{-i\omega(t-y/c)} \right\}, \quad (41)$$

where we have used again the definition of perturbation tensor (8) together with the components of the projector Λ_{ijkl} (5), $\Lambda_{xx,xx} = \Lambda_{zz,zz} = \frac{1}{2}$, $\Lambda_{zz,xx} = \Lambda_{xx,zz} = -\frac{1}{2}$, $\Lambda_{zx,zx} = \Lambda_{xz,xz} = 1$.

Again, the waves are linearly polarized as in the previous cases. The amplitudes of the polarization modes become, [32]:

$$A_+ = \frac{1}{r} \frac{G}{c^4} (\ddot{M}_{xx} - \ddot{M}_{zz}) = -\frac{1}{r} \frac{G}{c^4} S \rho_0 \left[a^2 \ddot{z}_s - (\dot{z}_s^3) \right],$$

$$A_\times = -\frac{2}{r} \frac{G}{c^4} \ddot{M}_{xz} = \frac{3}{2r} \frac{G}{c^4} S \rho_0 a (\dot{z}_s^2). \quad (42)$$

After we use the ansatz for the z_s we get

$$A_+ = \frac{6}{r} \frac{G}{c^4} S \rho_0 v_s^2 (f_1 - v_s t), \quad A_\times = \frac{3}{r} \frac{G}{c^4} S \rho_0 a v_s^2. \quad (43)$$

The resulting amplitudes A_+ and A_- have the same form as for the direction x (40) apart from the sign in A_\times . Importantly, the A_+ amplitude depends linearly on time and again the other one A_\times is constant in time. The amplitudes vanish as the radial distance $r \rightarrow \infty$ and decrease as $1/r$, the amplitude A_+ vanishes for time $t_{det} = f_1/v_s$ when the shock wave reaches the detector.

4.2 The general direction of the wave vector

Finally, we are going to investigate the amplitudes with the general wave vector of propagation.

The general direction of the wave propagation can be expressed in the spherical coordinates as

$$n = (\sin \theta \sin \phi, \sin \theta \cos \phi, \cos \theta), \quad (44)$$

and the perturbation tensor can be obtained via (8) and the projector (5).

The general expressions for the two modes of polarizations are, [32],

$$A_+(t; \theta, \phi) = \frac{1}{r} \frac{G}{c^4} \left[\ddot{M}_{xx} (\cos^2 \phi - \sin^2 \phi \cos^2 \theta) + \ddot{M}_{yy} (\sin^2 \phi - \cos^2 \phi \cos^2 \theta) - \ddot{M}_{zz} \sin^2 \theta \right. \quad (45)$$

$$\left. - \ddot{M}_{xy} \sin 2\phi (1 + \cos^2 \theta) + \ddot{M}_{xz} \sin \phi \sin 2\theta + \ddot{M}_{yz} \cos \phi \sin 2\theta \right], \quad (46)$$

$$A_\times(t; \theta, \phi) = \frac{1}{r} \frac{G}{c^4} \left[(\ddot{M}_{xx} - \ddot{M}_{yy}) \sin 2\phi \cos \theta - 2\ddot{M}_{xz} \cos \phi \sin \theta + 2\ddot{M}_{xy} \cos 2\phi \cos \theta + 2\ddot{M}_{yz} \sin \phi \sin \theta \right], \quad (47)$$

and the whole components of h_{ij}^{TT} can be expressed as (33) and (34). Afterwards we express mass moments in terms of derivatives of function z_s , the amplitudes read as follows,

$$A_+(t; \theta, \phi) = \frac{3}{4r} \frac{G}{c^4} S \rho_0 \left[\frac{4}{3} (\dot{z}_s^3) \sin^2 \theta + S \ddot{z}_s \sin 2\phi (1 + \cos^2 \theta) - (\dot{z}_s^2) \sin 2\theta (a \sin \phi + b \cos \phi) - \frac{4}{3} a^2 \ddot{z}_p (\cos^2 \phi - \sin^2 \phi \cos^2 \theta) - \frac{4}{3} b^2 \ddot{z}_p (\sin^2 \phi - \cos^2 \phi \cos^2 \theta) \right], \quad (48)$$

$$A_\times(t; \theta, \phi) = \frac{3}{2r} \frac{G}{c^4} S \rho_0 \left[(\dot{z}_s^2) \sin \theta (a \cos \phi - b \sin \phi) - S \ddot{z}_s \cos 2\phi \cos \theta + \frac{2}{3} (b^2 - a^2) \ddot{z}_s \sin 2\phi \cos \theta \right]. \quad (49)$$

After we use the ansatz for the z_s , we get

$$\begin{aligned} A_+(t; \theta, \phi) &= \frac{3G}{2c^4} S \rho_0 v_s^2 P_{A_+}(t; \theta, \phi), \\ A_\times(t; \theta, \phi) &= \frac{3G}{c^4} S \rho_0 v_s^2 P_{A_\times}(\theta, \phi), \end{aligned} \quad (50)$$

where the angular dependence is denoted as

$$\begin{aligned} P_{A_+}(t; \theta, \phi) &= \frac{1}{r} \{4(f_1 - v_s t) \sin^2 \theta - \sin 2\theta (a \sin \phi + b \cos \phi)\}, \\ P_{A_\times}(\theta, \phi) &= \frac{1}{r} \sin \theta (a \cos \phi - b \sin \phi). \end{aligned} \quad (51)$$

We obtained the amplitudes for two independent polarization modes with the general wave vector of propagation. We have included the r dependence in the angular parts of the amplitudes in order to investigate the dependence. The character of the amplitudes resembles the results from the two previous cases, the amplitude A_+ is linearly time dependent and the A_\times is constant in time. The amplitudes vanish as the radial distance $r \rightarrow \infty$ and decrease as $1/r$.

We will obtain the three previous cases as subcases of general amplitudes. The case $n_z = z$ (4.1.1) for $\theta = 0^\circ$, $\phi = 0^\circ$, the case $n_x = x$ (4.1.2) can be obtained for $\theta = 90^\circ$, $\phi = 90^\circ$ and case $n_y = y$ (4.1.3) for $\theta = 90^\circ$, $\phi = 0^\circ$.

The time when the shock wave reaches the detector is

$$t_{det} = f_1 / v_s. \quad (52)$$

We have used it to demonstrate the change in magnitude and in the geometrical structure of $P_{A_+}(t; \theta, \phi)$ and $P_{A_\times}(\theta, \phi)$. Such change can't be transformed away completely because it appears in the shifted coordinates ($f_1 = 0$) for $t = 0$, i.e. at the start of the propagation of the radiation.

In the following Figs., we will observe the effect of time dependence of the A_+ amplitude. The angular shape of $P_{A_+}(t; \theta, \phi)$ of the shock wave is depicted in Fig. 1 at start of the propagation, $t = 0$. The angular dependence has a symmetric shape of toroid with the center at $z = 0$ ($\theta = \phi = 0$). The surfaces inside of the toroid represent angular structure for larger r and we observe that the magnitude of the toroid becomes smaller, as expected, as $1/r$.

At the time shortly before the detector $t < t_{det}$, the angular dependence is smaller in Fig. 2 than the one in the previous Fig. 1 at $t = 0$ but the toroidal geometry remains. The Figs. were made for values $a = b = 10^{-3}$ m, $R_t = 15.14 \times 10^{-3}$ g/cm³ for Carbon, $I_L = 0.5 \times 10^{21}$ W/m² and $v_s = 1.55 \times 10^6$ m/s. Then the time when shock wave reaches detector is $t_{det} = 6.44 \times 10^{-5}$ s and the amplitudes become $A_{A_+} = 9.06 \times 10^{-36}$ and $A_{A_\times} = 1.81 \times 10^{-35}$.

At the moment t_{det} , when the shock wave reaches the detector, the first term in the angular dependence vanishes and the geometry of the angular dependence changes. In Fig. 3, we can see the structure of cloverleaf, the four leaves in four sectors, which is centered around $z = 0$. The surfaces for smaller r can be seen inside of the cloverleaf. We observe that the amplitude of the angular dependence is much smaller than the two previously pictured.

The amplitude for polarization mode \times is pictured in Fig. 4. Moreover, the spherical surface is pictured in the region where

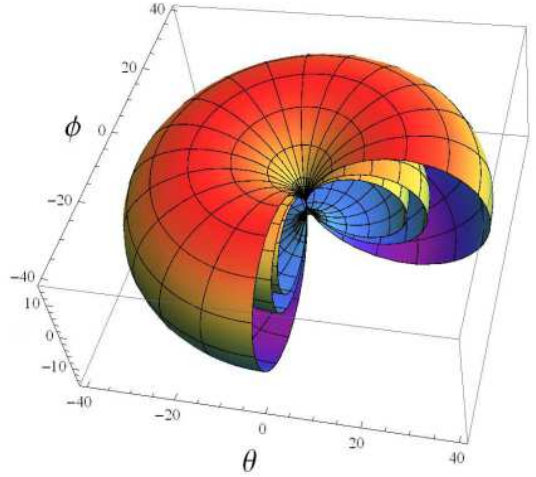


Figure 1. (Color online) The angular part of amplitude $P_{A_+}(t; \theta, \phi)$ (51) is pictured in dependence on θ and ϕ angle in radians at the time $t = 0$ in 3D figure. The amplitude has a shape of toroid with symmetry around axes $z = 0$. The dependence on $1/r$ is depicted in smaller surfaces in the figure, the biggest surface is $r = 1$ m, then $r = 1.5$ m and 1.8 m. The surface is getting smaller as $r \rightarrow 10$ m (at the distance of the detector) and approaches 0 as $r \rightarrow \infty$. The toroid was cut on purpose to see the inner surfaces of lower r .

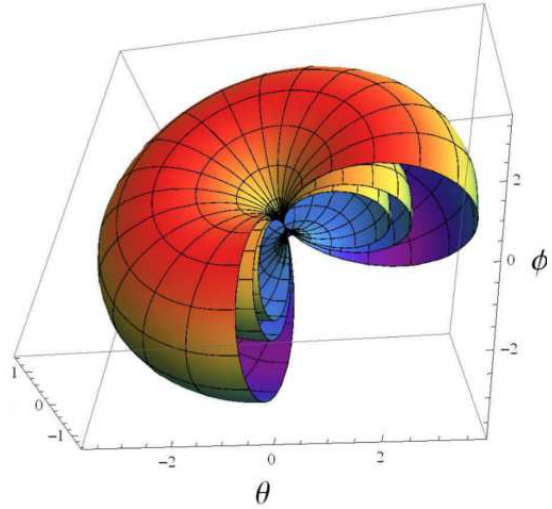


Figure 2. (Color online) The angular part of amplitude $P_{A_+}(t; \theta, \phi)$ (51) is pictured in dependence on θ and ϕ angle in radians at the time $t = 6 \times 10^{-5} < t_{det}$ s in 3D figure. The dependence on $1/r$ is depicted in smaller surfaces in the figure, the biggest surface is $r = 1$ m, then $r = 1.5$ m and 1.8 m. The surface is getting smaller as $r \rightarrow 10$ m (at the distance of the detector) and approaches 0 as $r \rightarrow \infty$. The magnitude of the diagram is significantly smaller than in the Fig. 1.

ϕ has negative values and θ has positive values in radians. It starts at $z = 0$, the sphere or bulb grows from that point. The shape stays the same during the experiment for all times. The measures are much smaller than the one in the images for the $+$ amplitude.

Interestingly, we investigate the orientation of both amplitudes with respect to each other, see the Fig. 5. In the first image, the amplitudes are compared some time before t_{det} and the

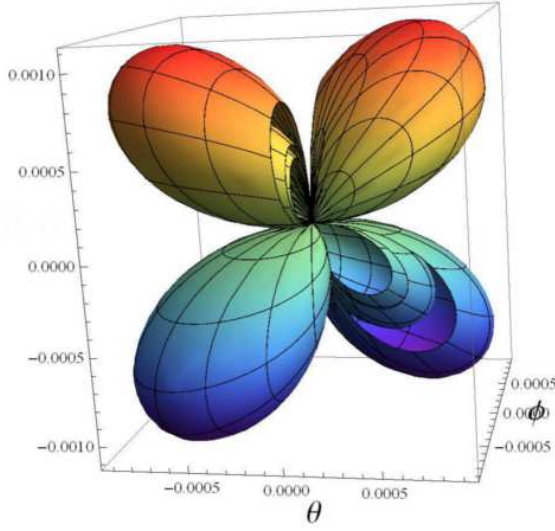


Figure 3. (Color online) The angular part of amplitude $P_{A_+}(t; \theta, \phi)$ (51) is pictured in dependence on θ and ϕ angle in radians at the detector in 3D figure. The geometry of toroid changed into cloverleaf geometry with symmetry around $z = 0$. The magnitude of the angular part of amplitude is much smaller than previous ones.

second image shows the amplitudes just at t_{det} , where the magnitude of amplitudes becomes similar.

The difference in the time dependency of the two independent polarization modes might be very important for the experimental detection, because it would be possible to distinguish the two modes of polarization. The one mode A_+ would be changing and getting smaller during the time of the experiment compared to the other, constant one A_\times , which could be measurable in principle.

4.3 The radiative characteristics for generated gravitational waves

The energy and momentum $t_{\mu\nu}^{GW}$ carried by the GWs at large distances from the source (at position of the detector) is described by the effective tensor

$$t_{\mu\nu}^{GW} = \frac{c^4}{32\pi G} \langle \partial_\mu h_{\alpha\beta} \partial_\nu h^{\alpha\beta} \rangle, \quad t_{00}^{GW} = \frac{c^4}{32\pi G} \langle \dot{A}_+^2 + \dot{A}_\times^2 \rangle, \quad (53)$$

where the brackets mean averaging over frequencies in one period of time, and the tensor (53) satisfies the energy conservation $\partial^\mu t_{\mu\nu} = 0$, [32, 33], and t_{00}^{GW} denotes gauge invariant energy density.

In our case, the A_\times amplitude is time-independent for our models, therefore just the A_+ contributes to the gauge density,

$$t_{00}^{GW} = \frac{c^4}{32\pi G} \langle \dot{A}_+^2 \rangle = \frac{9}{8\pi} \frac{G}{r^2 c^4} S^2 \rho_0^2 v_s^6 \sin^4 \theta, \quad (54)$$

which functionally depends on r and θ angle. The energy goes to zero as $r \rightarrow \infty$. The energy spectrum is then trivial $\frac{dE}{dA} = \frac{c^3}{16\pi G} \int_0^\tau dt \dot{A}_+^2 = \frac{c^3}{16\pi G} \dot{A}_+^2 \tau$ where $dA = r^2 d\Omega$ is surface element and τ is duration of pulse.

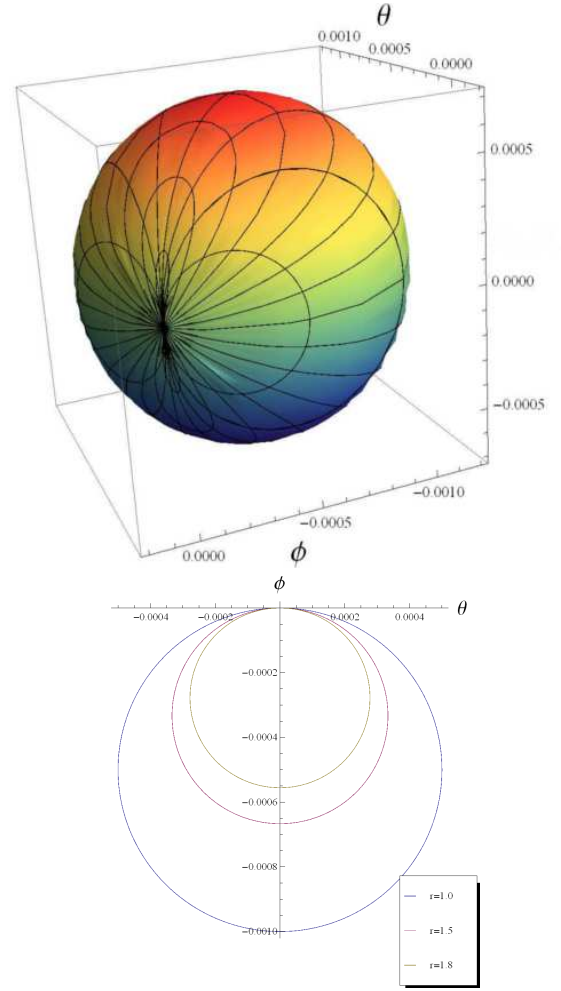


Figure 4. (Color online) The angular part of amplitude $P_{A_\times}(\theta, \phi)$ (51) is pictured in dependence on θ and ϕ angle in radians at any time. The surface is getting smaller as $r \rightarrow 10$ m (the distance of the detector) and approaches 0 as $r \rightarrow \infty$. The dependence on $1/r$ is depicted in smaller surfaces in the polar figure, the biggest surface is $r = 1$ m, then $r = 1.5$ m and 1.8 m where we have chosen $\phi = \pi/2$.

The radiative characteristic represents amount of energy going through various directions in the case of large distances r for quadrupole radiation. We can obtain it by using (53) and rewrite as

$$-t_{0r}^{GW} \equiv S = \frac{c^3}{72G\pi r^2} \langle \ddot{I}_{ij} \ddot{I}_{ij} - 2\ddot{I}_{is} \ddot{I}_{sj} n_i n_j + \frac{1}{2} \ddot{I}_{ij} \ddot{I}_{rs} n_i n_j n_r n_s \rangle. \quad (55)$$

The luminosity \mathcal{L}_{GW} defined in the beginning as (11) is connected to $t_{\mu\nu}^{GW}$ as $-\frac{dE}{dt} = \mathcal{L}_{GW} = \int t_{0r}^{GW} r^2 \sin \theta d\theta d\phi$, which can be found by integration over a sphere with diameter r .

We will express the Eq. (55) for the orientation of wave vector into x , y and z directions.

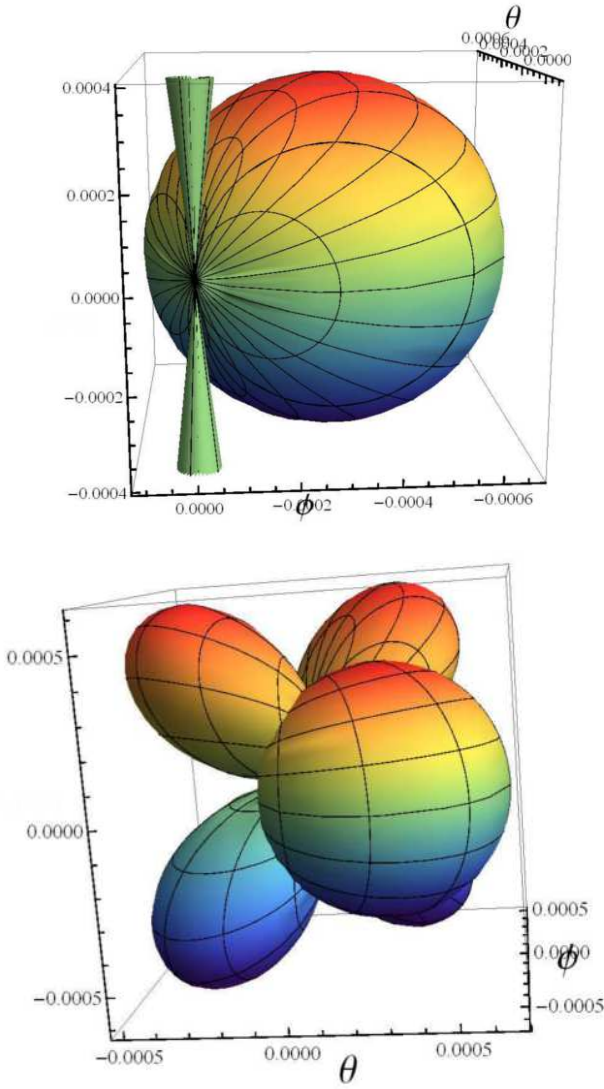


Figure 5. (Color online) The angular part of amplitude $P_{A_+}(t; \theta, \phi)$ and $P_{A_x}(\theta, \phi)$ (51) is pictured in dependence on θ and ϕ angle in radians together in two figures for comparison at different times. In the first figure at $t < t_{det}$, the amplitude A_x is rather small compared to the A_+ central part of toroid. In the second figure at t_{det} , both amplitudes become comparable at the detector. The figures are made for $r = 1.8$ m.

The expression (55) for the orientation of the wave vector to x, y, z direction reads,

$$S_{n_x} = \frac{c^3}{72G\pi r^2} \left[-\frac{1}{2}(\ddot{I}_{xx})^2 + (\ddot{I}_{yy})^2 + (\ddot{I}_{zz})^2 + 2(\ddot{I}_{yz})^2 \right], \quad (56)$$

$$S_{n_y} = \frac{c^3}{72G\pi r^2} \left[(\ddot{I}_{xx})^2 - \frac{1}{2}(\ddot{I}_{yy})^2 + (\ddot{I}_{zz})^2 + 2(\ddot{I}_{xz})^2 \right], \quad (57)$$

$$S_{n_z} = \frac{c^3}{72G\pi r^2} \left[(\ddot{I}_{xx})^2 - \frac{1}{2}(\ddot{I}_{yy})^2 + (\ddot{I}_{zz})^2 + 2(\ddot{I}_{xz})^2 \right]. \quad (58)$$

We can evaluate (55) for the general wave vector (44) as

$$S_n = \frac{c^3}{72G\pi r^2} \left[(\ddot{I}_{xx})^2(1 - 2 \sin^2 \theta \sin^2 \phi) \right. \\ \left. + (\ddot{I}_{yy})^2(1 - 2 \sin^2 \theta \cos^2 \phi) + (\ddot{I}_{zz})^2(1 - 2 \cos^2 \theta) \right. \\ \left. + \frac{1}{2} (\ddot{I}_{xx} \sin^2 \theta \sin^2 \phi + \ddot{I}_{yy} \sin^2 \theta \cos^2 \phi + \ddot{I}_{zz} \cos^2 \theta)^2 \right], \quad (59)$$

where the expression simplifies since $\ddot{I}_{xy} = \ddot{I}_{xz} = \ddot{I}_{yz} = 0$.

Now, we are able to substitute the ansatz for the z_s into (56), (57), (58) and (59). Then the expressions for the wave vector in directions n_x, n_y, n_z read,

$$S_{n_x} = \frac{c^3}{4G\pi r^2} S^2 \rho_0^2 v_s^6, \quad S_{n_y} = \frac{c^3}{4G\pi r^2} S^2 \rho_0^2 v_s^6, \quad S_{n_z} = 0,$$

and the expression for the general wave vector (44) results in

$$S_n = A_{S_n} P_{S_n}(\theta, r), \quad A_{S_n} = \frac{S^2 c^3 \rho_0^2 v_s^6}{36G\pi}, \quad (60)$$

where the angular dependence is given as

$$P_{S_n}(\theta, r) = \frac{1}{r^2} \left[12 - 4(\sin^2 \theta + 4 \cos^2 \theta) + (2 \cos^2 \theta - \sin^2 \theta)^2 \right]. \quad (61)$$

The radiative characteristics (61) depends only on the θ angle which is a consequence of the axial symmetry of the problem. It behaves as $1/r^2$ as $r \rightarrow \infty$ contrary to $1/r$ decay of amplitudes.

The radiation structure is pictured in Fig. 6, where the structure of the surface corresponds to toroidal shape similar to the amplitudes (51). The extreme values of the function $P_{S_n}(\theta, r)$ of the angle θ correspond to the values of θ where $\sin 2\theta = 0$ or $2/3 = \cos^2 \theta + \cos 2\theta$.

The amplitude $A_{S_n} = \frac{S^2 c^3 \rho_0^2 v_s^6}{36G\pi}$ (60) has a specific value $A_{S_n} = 1.49 \times 10^{53}$ for $a = b = 10^{-3}$ m, $R_t = 15.14$ kg/m³ for Carbon, $I_L = 0.5 \times 10^{21}$ W/m² and $v_s = 1.55 \times 10^6$ m/s. The polar dependence on θ, ϕ and r is plotted in Fig. 6 and the dependence on θ and r is plotted in Fig. 7.

This directional characteristic tells us, in fact, where to expect the gravitational radiation and where not, therefore it is one of the main results of the paper. The experimental set up and positions of the detectors should be adjusted to the directional characteristic to make the experiment the most effective.

4.4 The angular momentum

The gravitational waves carry away energy and angular momentum, the angular momentum carried away per unit time by the gravitational waves is given by using the derivatives quadrupole moment as

$$\left(\frac{dJ^i}{dt} \right)_{quad} = \frac{2G}{5c^5} \epsilon^{ijkl} \ddot{I}_{ka} \ddot{I}_{la} \rightarrow 0, \quad J^i = \text{const}, \quad (62)$$

where the derivatives of the quadrupole moment are evaluated at the retarded time $t - r/c$, [4, 32].

The angular momentum of the radiation in the shock wave model stays constant in time. Which is due to the linear movement of shock wave. The situation will be different in case of rotating stick or double-star.

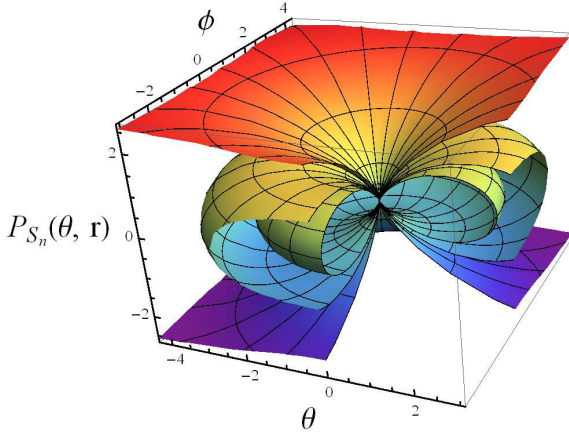


Figure 6. (Color online) The radiation characteristics S_n (60) is pictured in dependence on θ angle and rotated additionally around ϕ angle in radians. We have plotted just the angular dependence $P_{S_n}(\theta, r)$ (61), $S_n = A_{S_n} P_{S_n}(\theta, r)$, (60). The dependence on $1/r^2$ is depicted in smaller surfaces in the figure, the biggest surface is for $r = 1$ m, then $r = 1.5$ m, 1.8 m. The surface is getting smaller as $r \rightarrow 10$ m (the distance of the detector), while $r \rightarrow \infty$ the surface approaches 0. The structure of surfaces is symmetric around the axes $z = 0$. The structure of the surface has similar shape as the amplitudes.

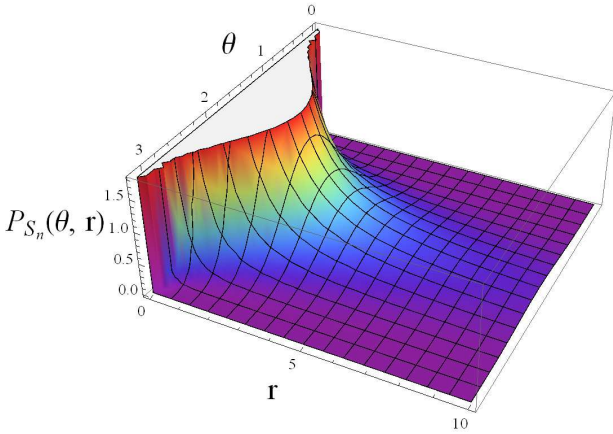


Figure 7. (Color online) The radiation characteristics S_n (60) is pictured in polar coordinates θ in radians and r in meters. Just the angular dependence is plotted $P_{S_n}(\theta, r)$ (61). The radiation tends to small values for $r = 10$ m and vanishes at infinity.

5 The behavior of test particles in the presence of a gravitational wave

In this Sect. we investigate the influence of the gravitational field of gravitational wave on two close particles and the equation of motion, called the equation of deviation, in local reference frame by analysing the distance of two particles for our models. The equation of deviation is defined as

$$\frac{d^2 x_B^j}{dt^2} = -R_{j0k0} x_B^k = \frac{1}{2} \frac{\partial^2 h_{jk}^{TT}}{\partial t^2} x_B^k, \quad (63)$$

which describes the relative acceleration of two particles originally moving along two parallel trajectories in proper detec-

tor frame. We have used the fact that to first order in h_{ij}^{TT} , $t = \tau + O(h)$. The equation (63) can be integrated if we assume that the particles are at rest relative to each other before the wave arrives (when $h_{ij}=0$ then $x_B^j = x_{B(0)}^j$). The equation of motion yields $x_B^j(\tau) = x_{B(0)}^k \left[\delta_{jk} + \frac{1}{2} h_{jk}^{TT}(\tau) \right]_{\text{at position of A}}$ and describes the oscillations of particle B's location measured in the reference frame of particle A. The position of the second particle B can be affected by the wave just in traversal directions to the wave propagation direction.

5.1 The predictions for the detector

The equation of deviation (63) is valid as long as $|x_B|$ is much smaller than typical scale over which the gravitational field changes substantially. For GW, the length scale is the reduced wavelength λ and the estimate for the detector L (typical scale) is

$$L \ll \lambda \rightarrow L \ll 0.21 \times 10^{-1} \text{ m}, \quad (64)$$

where $\lambda = \lambda/2\pi$ is reduced wavelength of the gravitational wave and L is the detector's characteristic linear size L . This might serve as useful estimation for validity of the future experiment and the detector. We have used the numerical values mentioned in Subsect. (3.2). If the condition (64) is not satisfied the full relativity approach would be necessary. For example, the bar detectors and ground based interferometers satisfy (in the first approximation) this condition but LISA does not.

5.2 Movement of particles

First, we will investigate the effect of the linearly polarized gravitational wave on test particles in the mode + for the wave vector in x direction (4.1.2) because the case for z direction is trivial. Since the propagation of the laser occurs in the z direction and the wave vector is oriented in the x coordinate, the movement will happen in the (z, y) plane. We assume that the test particles are set on a circle of radius $r = a$ at time $\tau = 0$. In the center of the circle is the reference particle A, which is at rest in the proper reference frame. The position of the particle in any time is defined by (63). We will denote the coordinates in the reference frame as \tilde{x} , \tilde{y} and \tilde{z} , then we will get for near particle in time τ (for $A_x = 0$),

$$\begin{aligned} \tilde{z}_B(\tau) &= \left[1 + \frac{1}{2} h_{zz}^{TT}(\tau) \Big|_{\tilde{x}_A^j=0} \right] \tilde{z}_{B(0)}, \\ \tilde{y}_B(\tau) &= \left[1 - \frac{1}{2} h_{zz}^{TT}(\tau) \Big|_{\tilde{x}_A^j=0} \right] \tilde{y}_{B(0)}, \end{aligned} \quad (65)$$

where we have used $h_{zz}^{TT} = -h_{yy}^{TT}$, $z_{B(0)} = a \cos \phi$ and $y_{B(0)} = a \sin \phi$ which are coordinates in time $\tau = 0$ when the particles were distributed along the circle of radius a . In the further text, we assume all $h_{ij}^{TT} \Big|_{\tilde{x}_A^j=0}$ (i.e. are evaluated at $\tilde{x}_A^j = 0$) and we will not write it explicitly.

The expression $\cos^2 \phi + \sin^2 \phi = 1$ then leads to $\left\{ \frac{\tilde{z}_B(\tau)}{a[1+\frac{1}{2}h_{zz}(\tau)]} \right\}^2 + \left\{ \frac{\tilde{y}_B(\tau)}{a[1-\frac{1}{2}h_{zz}(\tau)]} \right\}^2 = 1$, which is equation of ellipse with semi-minor

axes $a[1 \pm \frac{1}{2}h_{zz}(\tau)]$. The reference frame has origin at $\tilde{x} = \tilde{y} = \tilde{z} = 0$ and in the coordinates of TT gauge $x = y = 0$ and $z = f_1$ and $t = \tau + O(h)$. For convenience, we will shift the origin of the coordinates to $z = f_1$, then the coordinates of TT gauge will be $x = y = 0$ and $z = 0$ and $t = \tau + O(h)$.

Recall that we take real part of $h_{zz}^{TT}(z), h_{zz}(\tau) = \text{Re}\{A_+ e^{-i\omega\tau}\} = (\text{Re} A_+) \cos \omega\tau - (\text{Im} A_+) \sin \omega\tau$, where we observe that $\text{Im} A_+ = 0$ then $h_{zz}(\tau) = A_+ \cos \omega\tau$. Without losing any information, we perform a phase shift, $+\pi/2$, and get $h_{zz}(\tau) = A_+ \sin \omega\tau$. Otherwise the component $h_{zz} = g(f_1)$ will be non-zero. Now, when $\tau = 0$ then $h_{zz} = h_{zz}(\tau) = 0$.

The semi-minor axes are $a[1 \pm A \sin \omega\tau]$, where $A = \frac{1}{2}A_+$ and

$$A \equiv A|_{\tilde{x}_A=0} = \frac{3}{r} \frac{G}{c^4} S \rho_0 v_s^2 (-v_s \tau),$$

$$\frac{1}{2} h_{zz}^{TT}(\tau)|_{\tilde{x}_A=0} = \frac{3}{r} \frac{G}{c^4 \omega} S \rho_0 v_s^2 (-v_s \omega \tau) \sin \omega\tau. \quad (66)$$

The initial position of test particles on circle is pictured in Fig. 8(a) at $\tau = 0$, then the circle is gradually changing into ellipse Fig. 8(b) due to the influence of the wave, into the direction of \tilde{y}_B , then it changes to back to circle Fig. 8(c), then again into prolonged ellipse \tilde{z}_B Fig. 8(d) and then it gets back to circle (Fig. 8(a)). In our specific case, the ellipse is changing its shape due to the time dependency of the amplitude A_+ .

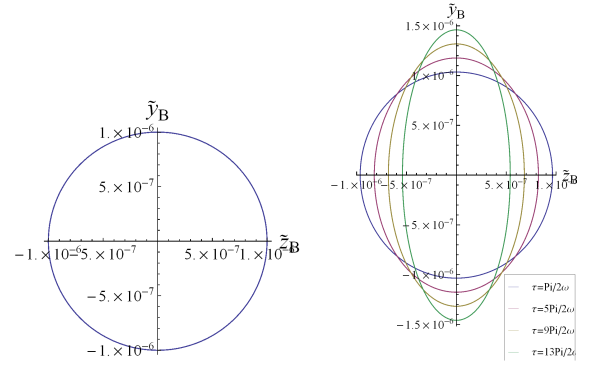
In Figs. 8(b) and 8(d), the time dependence of the amplitude is demonstrated explicitly. In Fig. 8(b), we observe the changing of the ellipse to a sharper profile as the time grows, in Fig. 8(d) the ellipse gets sharper profile in the transversal direction.

For demonstrational purposes, we have used $\frac{1}{2} h_{zz}^{TT}(\tau)|_{\tilde{x}_A=0} = -0.45 \omega \tau \sin \omega\tau$ to make the effect of time dependent amplitude visible. The real value is very small and difficult to plot. For example, for specific values, $a = b = 10^{-3} \text{m}$, $R_t = 15.14 \text{kg/m}^3$ for Carbon, $I_L = 0.5 \times 10^{21} \text{W/m}^2$, $v_s = 1.55 \times 10^6 \text{m/s}$, $\omega = 2\pi c/\lambda = 6.26 \times 10^9$ where $\lambda = 0.3 \text{m}$, we get the real estimate for the amplitude $A = -2.81 \times 10^{-31} \tau$.

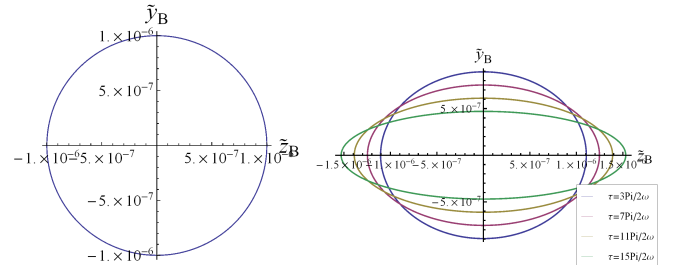
In the mode \times , we will get also deformation of a circle with the only non-zero component h_{zy}^{TT} . Its amplitude reads $\frac{1}{2} h_{yz}^{TT}(\tau)|_{\tilde{x}_A=0} = -\frac{3}{r} \frac{G}{c^4} S \rho_0 v_s^2 \sin \omega\tau$, while we have used function $\frac{1}{2} h_{yz}^{TT}(\tau)|_{\tilde{x}_A=0} = -5 \sin \omega\tau$ contrary to the real value $\frac{1}{2} h_{yz}^{TT}(\tau)|_{\tilde{x}_A=0} = -9.05 \times 10^{-40} \sin \omega\tau$ evaluated using parameters above. The value is significantly smaller than the value of amplitude from the previous case therefore we observe that the two polarizations might be very easy to distinguish in the experiment. The component h_{yz}^{TT} has constant amplitude therefore the ellipses do not change shape when time grows. In the Fig. 9, the diagrams are plotted to demonstrate the movement of test particles in e_\times polarization. The ellipses are rotated by 45° compared to Fig. 8.

6 Conclusion

We have investigated models for the generation of gravitational waves in three different experiments in laboratory conditions. The models for experiments are based on high power laser-matter interaction. In this paper, we concentrate on the shock wave model.



(a) The test particles at $\tau = 0$, (b) The test particles at $\tau = \pi/2\omega, 5\pi/2\omega, 9\pi/2\omega, 13\pi/2\omega$ and more.



(c) The test particles at $\tau = \pi/\omega, 3\pi/\omega, 5\pi/\omega$ and more. (d) The test particles at $\tau = 7\pi/2\omega, 11\pi/2\omega, 15\pi/2\omega$ and more.

Figure 8. (Color online) The diagrams depict the position of test particles as function of time under influence of GW wave with + polarization.

We have verified that linear gravity can be used for the shock wave model, calculated and analyzed the perturbation tensor h_{ij}^{TT} and the luminosity of gravitational radiation \mathcal{L}_{GW} in low velocity approximation far away from the source. The calculations are presented in detail and estimations for real experimental values with megajoule class lasers are $\mathcal{L}_{GW} \approx 1.69 \times 10^{-29} [\text{W}]$, $h_{zz}^{GW} \approx 2.37 \times 10^{-39}$. The orders of h_{zz} correspond to [7,8] but the order of \mathcal{L}_{GW} is four orders lower. The results presented in [7,8] were generalized to include the dependence on the laser wavelength and material of the foil.

We have also investigated the two independent polarization modes of the gravitational radiation in the shock wave model. The amplitudes of the radiation were derived in the three main directions of wave propagation, x, y, z . The radiation vanishes in the direction of motion in the z direction. The amplitude for mode $+$ of the polarization occurs as time dependent and the other amplitude for mode \times is time-independent. The geometrical shape of the amplitude is toroid for A_+ (Fig. 1), and a bulb for A_\times (Fig. 4).

Furthermore, the radiative characteristics in the general wave direction given by angles θ and ϕ was investigated. The obtained directional structure has toroidal shape, see Fig. 6, and has symmetry around $z = 0$ axes and decreases with distance from the source of radiation as $1/r^2$. This result could help with the positioning of the detectors in the experiment and make it the most effective.

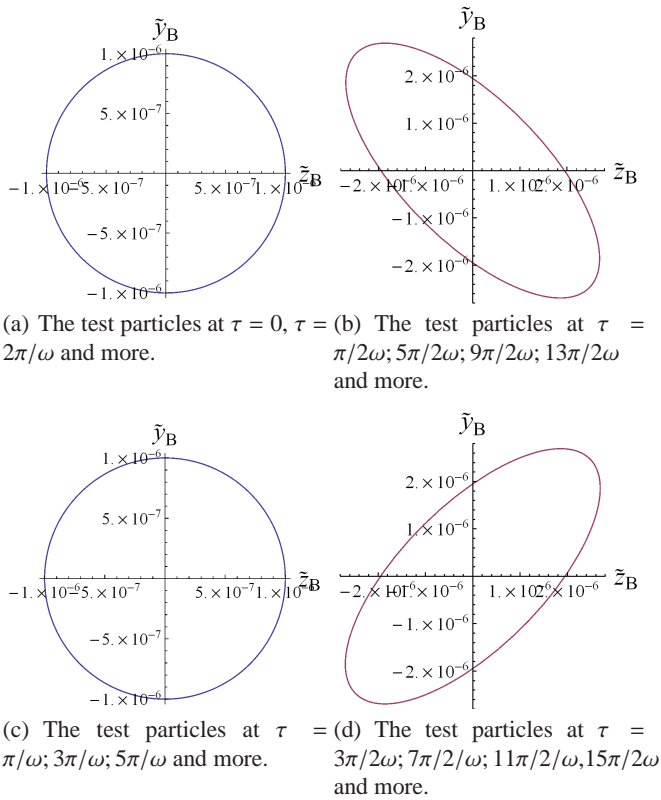


Figure 9. (Color online) The diagrams depict the position of test particles as function of time under influence of GW wave with \times polarization.

Then the influence of gravitational waves was analyzed on test particles using the geodesics equation. The difference in amplitudes of the two modes of polarization was demonstrated and visualized in detail, see Figs. 8 and 9. The time dependent amplitude of polarization + influences the circle of particles to change the shape to ellipse and as time is passing the ellipse shape becomes sharper. The \times polarization of the GW influences the circle of test particles to change the shape to ellipse shifted by 45° and the shape stays constant in time. The changes in the shape of the test particles could be in principle measurable in an experiment.

Therefore the remaining problem is the detection of the gravitational waves which have the amplitude of the metric perturbation around 10^{-40} which is almost 20 orders lower than the detected radiation from space [2]. The frequencies are in the GHz – THz range therefore the gravitational waves can't be detected by any of the known detectors like interferometers or the Weber resonators. The suggested Li–Baker detector is one candidate for the detection of high frequency waves (10 GHz) because it uses a different technology. Further improvement of detectors in higher frequency range might enable the measurement of the gravitational waves produced by the presented models.

H. Kadlecová wishes to thank Tomáš Pecháček for many valuable discussions and time, and Otakar Svítek for his valuable comments. The

work was supported by the ELI project No. CZ.02.1.01./0.0/0.0/15-008/0000162.

References

1. A. Einstein, Sitz. Preuss. Akad. Wiss. (Berlin), (1918) 154–167.
2. B. P. Abbott et al., Phys. Rev. Lett. **116**, (2016) 061102.
3. R. A. Hulse, J. H. Taylor, Astr. Phys. J **L51**, (1975) 195.
4. C. W. Misner, K. S. Thorne, J. A. Wheeler, *Gravitation* (W. H. Freeman and Company, 1973).
5. J. F. Chapline, Phys. Rev. D **10**, (1974) 1064.
6. V. N. Rudenko, Grav. Cosmol. **10**, (2004) 41.
7. X. Ribeyre, V. T. Tikhonchuk, in *Proceedings of 12th Marcel Grossmann Meeting on General Relativity, Paris, 2009*, edited by T. Damour, R. T. Jantzen and R. Ruffini, World Scientific, 2012, 1640–1642.
8. X. Ribeyre, V. T. Tikhonchuk, in *Presentation on IZEST-ELI-NP Conference, Paris, 2014*.
9. J. Weber, Phys. Rev. **117**, (1960) 306.
10. H. A. de Waard, L. Gottardi, J. van houwelingen, A. Shumack, G. Frossati, Class. Quant. Grav. **20**, (2003) S143–S151.
11. See <http://www.auriga.lnl.infn.it/>.
12. M. Cerdonio et al., Class. Quant. Grav. **14**, (2003) 1491.
13. See <http://www.ligo.org/>
14. T. T. Fricke et al., Class. Quant. Grav. **29**, (2012) 065005.
15. See <http://www.cascina.virgo.infn.it/>.
16. V. B. Braginskij, Phys. Usp. **43**, (2000) 691.
17. See <http://lisa.nasa.gov/>.
18. K. Yagi, Int. J. Mod. Phys. D **22**, (2013) 1341013.
19. See <http://www.geo600.org>
20. K. Tang et al., in *Proceedings of Radio Science Conference, Qingdao, China, 2004*, edited by T. Keyun and L. Dayong, Piscataway, N.J. : IEEE, Beijing, China : Pub. House of Electronics Industry.
21. R. Baker Jr., R. C. Woods, F. Li, in *Proceedings of Space Technology and Applications International Forum (STAIF-2006), 2006*, edited by M. S. El-Genk, American Institute of Physics Conference Proceedings (Melville, NY), 1280-1289.
22. F. Li, H. Wen, Z. Fang, Chinese Physics B **22**, (2013) 120402.
23. F. Li et al., Phys. Rev. D **80**, (2009) 064013.
24. A. Arvanitaki, A. A. Geraci, Phys. Rev. Lett. **110**, (2013) 071105.
25. R. Fabbro, C. Max, E. Fabre, Phys. Fluids **25**, (1984) 5.
26. N. Naumova et al., Phys. Rev. Lett. **102**, (2009) 025002.
27. E. Gelfer, H. Kadlecová, O. Klimo, S. Weber, G. Korn, Physics of Plasmas **23**, (2016) 093107.
28. R. Baker, F. Y. Li, in *Proceedings of Space Technology and Applications International Forum (STAIF-2005), 2005*, edited by M. S. El-Genk, American Institute of Physics Conference Proceedings (Melville, NY).
29. F. Li, R. Baker, Presentation on www.gravwave.com, *Development of the Li–Baker ultra–high sensitivity high frequency relic gravitational wave detector, 2011*.
30. M. E. Gertsenshtein, Sov. Phys. JETP **14**, (1962) 84.
31. See <https://fas.org/trp/agency/dod/jason/gravwaves.pdf>.

32. M. Maggiore, *Gravitational waves: Volume I: Theory and Experiments* (Oxford university Press, NY, 2008).
33. J. Bičák, V. N. Rudenko, *Teorie relativity a gravitační vlny* (MFF UK, Prague, 1986).
34. S. Atzeni, J. Meyer–Ter–Vehn, *Physics of Inertial Fusion* (Clarendon Press–Oxford, Oxford, 2004).
35. E. M. Campbell, W. J. Hogan, *Plasma Phys. Controll. Fusion* **41 (12B)**, (1999) B39.
36. J.–L. Miquel, C. Lion, P. Vivini, *J. Phys.: Conf. Series* **688**, (2016) 012067.

